NUMERICAL SIMULATION OF THE LAMINAR TRANSONIC BUFFET IN AIRFOILS

Roberto F. Bobenrieth Miserda
Universidade de Brasília, ENM – FT – UnB, Campus Universitário, Asa Norte, Brasília, DF, 70910-900, Brasília, DF, Brasil
rfbm@unb.br

Jean Rafael Jalowitzki
Universidade de Brasília, ENM – FT – UnB, Campus Universitário, Asa Norte, Brasília, DF, 70910-900, Brasília, DF, Brasil
j0052019@aluno.unb.br

Rúdner Lauterjung Queiroz
Universidade de Brasília, ENM – FT – UnB, Campus Universitário, Asa Norte, Brasília, DF, 70910-900, Brasília, DF, Brasil
r0015687@aluno.unb.br

Alessandra Freire de Mendonça
Universidade de Brasília, ENM – FT – UnB, Campus Universitário, Asa Norte, Brasília, DF, 70910-900, Brasília, DF, Brasil
afmend@engineer.com

Abstract. *The objective of this work is the numerical simulation of the shock wave-boundary layer interaction that appears in the transonic regime for the laminar flow in a NACA 0012 airfoil. The compressible Navier-Stokes equations are numerically solved using a finite volume discretization in combination with the skew-symmetric form of Ducros' fourth-order numerical scheme. Results are obtained for angles of attack ranging from 0 to 9 degrees and for a Reynolds number of 10,000. For low angles of attack, the visualization shows the acoustics waves generated by a mild separation of the boundary layers along the upper and lower surface and the subsequent von Kármán's vortex street. As the angle of attack increases, the acoustic waves turn into shock waves and a strong separation of the boundary layer is induced, generating a more complex vortex wake. The results also show a strong variation in the resultant unsteady aerodynamic coefficients. For low angles of attack, the unsteady normal force coefficient is characterized by a characteristic amplitude and frequency. As the angle of attack increases to a limit of 7 degrees, a strong shock wave-boundary layer interaction appears producing an increment of the amplitude of the normal force coefficient in conjunction with a reduction of the characteristic frequency. For 9 degrees of angle of attack, the unsteady normal force coefficient shows a departure, characterized by more than one characteristic frequency.*

Keywords. *NACA 0012 airfoil, transonic buffet, laminar flow, compressible flow.*

1. Introduction

This work is aimed at the numerical simulation of the strong shock-boundary layer interaction that arises in the transonic flow over NACA 0012 airfoil in laminar regime over a range of angles of attack. This kind of interaction is the cornerstone of the transonic-buffet phenomenon, of keen interest in the aerospace sciences. Due to the complex nature of the shock-boundary layer interaction, not every numerical method is able to tackle this type of problems. Only shock-capturing schemes can obtain meaningful results. One drawback of this type of methods is the tendency to over dissipate in regions that are not shock waves, such as high shear-stress regions, resulting in the dumping of the phenomenon. In this work, a new type of sensor, proposed by Ducros et al. (1999) is used for appropriately triggering the artificial dissipation in order to minimize this problem.

The effect of the Mach number over the laminar transonic flow over a NACA 0012 airfoil was studied by Bouhadji and Braza (2003). The focus of that work was the analysis of the resulting organized modes from the boundary layer-acoustic wave and boundary layer-shock wave interaction. To perform that analysis, the angle of attack was fixed to 0 degrees and the numerical simulation was carried out with a Mach number ranging from 0.20 to 0.98. Acoustic waves gave place to shock waves as the Mach number increased. In order to complement that effort, in the present work, the Mach number is fixed to 0.80 and the simulation is carried out for angles of attack ranging from 0 to 9 degrees. This is done in order to determine the angle of attack where the acoustic waves, associated to low angles of attack for a Mach number of 0.80, gave place to shock waves, associated with higher angles of attack at the same Mach number.

From the methodological point of view, the numerical simulation of vortex-shock interactions has been the focus of many recent works. Yee et al. (1999) proposed a family of low-dissipative and high-orders shock-capturing methods using characteristic-based filters to minimize the numerical dissipation of the overall scheme. This methodology was successfully applied to the simulation of the vortex pairing in a time-developing laminar mixing layer, the shock-wave impingement on a spatially evolving laminar mixing layer and a compressible turbulent channel flow. The former two

problems were also solved by Yee et al. (2000) using an entropy-splitting approach. This approach was also used by Sandham et al. (2002) in the numerical simulation of the compressible channel flow. The idea of a skew-symmetric splitting was presented by Yee and Sjogreen (2001) and used to simulate the complex two-dimensional shock/boundary-layer interaction in the laminar problem proposed by Daru and Tenaud (2001). All the above works used a finite-difference discretization. Ducros et al. (2000) proposed a family of high-order fluxes for conservative skew-symmetric-like schemes using structured meshes that can be used by a finite-difference or a finite-volume discretization. In this work, Ducros' fourth-order skew-symmetric scheme for a finite-volume discretization in conjunction with a third-order Runge-Kutta time-marching method is used. The resulting numerical scheme is fourth-order accurate in space and third-order accurate in time.

2. Mathematical Model

The nondimensional form of the compressible Navier-Stokes equations can be written as:

$$\frac{\partial \rho}{\partial t} + \frac{\partial}{\partial x_i}(\rho u_i) = 0 \, , \tag{1}$$

$$\frac{\partial}{\partial t}(\rho u_i) + \frac{\partial}{\partial x_j}(\rho u_i u_j) = -\frac{\partial p}{\partial x_i} + \frac{\partial \tau_{ij}}{\partial x_j} \, , \tag{2}$$

$$\frac{\partial}{\partial t}(\rho e_T) + \frac{\partial}{\partial x_i}(\rho e_T u_i) = -\frac{\partial}{\partial x_i}(p u_i) + \frac{\partial}{\partial x_i}(\tau_{ij} u_j) - \frac{\partial q_{x_i}}{\partial x_i} \, . \tag{3}$$

All the variables are in nondimensional form and have their usual meaning, i.e., x_i is the i-direction spatial coordinate, t is the temporal coordinate, ρ is the density, u_i is the i-direction component of the velocity vector, p is the thermodynamic pressure, T is the temperature, e is the internal specific energy, μ is the viscosity, c_v is the specific heat at constant volume, τ_{ij} is the viscous stress tensor, e_T is the total specific energy and q_{x_i} is i-direction of the heat-flow density vector. The nondimensional form for all the variables is defined using the following procedure:

$$x_i = \frac{x_i^*}{L^*}, \quad u_i = \frac{u_i^*}{U_\infty^*}, \quad t = \frac{t^*}{L^*/U_\infty^*}, \quad p = \frac{p^*}{\rho_\infty^*(U_\infty^*)^2}, \quad \rho = \frac{\rho^*}{\rho_\infty^*}, \quad T = \frac{T^*}{T_\infty^*}, \quad e = \frac{e^*}{(U_\infty^*)^2}, \quad \mu = \frac{\mu^*}{\mu_\infty^*}, \quad c_v = \left[\frac{T_\infty^*}{(U_\infty^*)^2}\right] c_v^*, \tag{4}$$

where U_∞^* is the velocity magnitude of the undisturbed flow, L^* is the characteristic length of the problem, the superscript * represents dimensional variables and the subscript ∞ stands for undisturbed-flow properties.

The viscous-stress tensor is given by

$$\tau_{ij} = \frac{1}{\text{Re}}\left(\mu S_{ij}\right) = \frac{1}{\text{Re}}\left\{\mu\left[\left(\frac{\partial u_i}{\partial x_j} + \frac{\partial u_j}{\partial x_i}\right) - \frac{2}{3}\delta_{ij}\frac{\partial u_k}{\partial x_k}\right]\right\} \, , \tag{5}$$

where S_{ij} is the nondimensional rate-of-strain tensor, δ_{ij} is the Kronecker delta and the Reynolds number is defined as

$$\text{Re} = \frac{\rho_\infty^* U_\infty^* L^*}{\mu_\infty^*} \, . \tag{6}$$

The total energy is given by the sum of the internal and kinetic specific energy as

$$e_T = e + e_k = c_v T + \frac{u_i u_i}{2} \, , \tag{7}$$

and the heat-flux density is

$$q_{x_i} = -\frac{\mu}{(\gamma - 1)M^2 \, \text{Re} \, \text{Pr}}\left(\frac{\partial T}{\partial x_i}\right) \, , \tag{8}$$

where γ is the specific-heat ratio and the Mach and Prandtl numbers are respectively defined as

$$M = \frac{U_\infty^*}{\sqrt{\gamma R^* T_\infty^*}}, \qquad \mathrm{Pr} = \frac{c_p^*}{k_\infty^*} \mu_\infty^*.$$ (9)

In this work, the Prandtl number is considered a constant with the value $\mathrm{Pr} = 0.72$. For a thermally and calorically perfect gas, the nondimensional equation of state can be written as

$$p = (\gamma - 1)\rho e$$ (10)

and

$$T = \frac{\gamma M^2 p}{\rho}.$$ (11)

The nondimensional molecular viscosity is obtained using Sutherland's formula

$$\mu = C_1 \frac{T^{3/2}}{T + C_2}, \qquad C_1 = \left[\frac{\left(T_\infty^*\right)^{1/2}}{\mu_\infty^*}\right] C_1^*, \qquad C_2 = \frac{C_2^*}{T_\infty^*},$$ (12)

where C_1^* and C_2^* are dimensional constants.

The boundary conditions at the wall of the two-dimensional base are a no-slip condition for the velocity field, an adiabatic wall for the temperature field and a null gradient in the normal direction at the wall for the pressure field.

3. Numerical Method

Since the geometry of interest is a two-dimensional base and the flow around it is laminar, the two-dimensional form of the Navier-Stokes is used. In order to numerically solve this equations using a finite volume approach, Eqs. (1), (2) and (3) are written in the following vector form (Anderson et al., 1983):

$$\frac{\partial \mathbf{U}}{\partial t} + \frac{\partial \mathbf{E}}{\partial x} + \frac{\partial \mathbf{F}}{\partial y} = \mathbf{0},$$ (13)

where the conservative-variables vector $\mathbf{U}$, and the flux vectors $\mathbf{E}$ and $\mathbf{F}$ are given by

$$\mathbf{U} = \begin{bmatrix} \rho \\ \rho u \\ \rho v \\ \rho e_T \end{bmatrix}, \quad \mathbf{E} = \begin{bmatrix} \rho u \\ \rho u^2 + p - \tau_{xx} \\ \rho u v - \tau_{xy} \\ (\rho e_T + p)u - u\tau_{xx} - v\tau_{xy} + q_x \end{bmatrix}, \quad \mathbf{F} = \begin{bmatrix} \rho v \\ \rho v u - \tau_{xy} \\ \rho v^2 + p - \tau_{yy} \\ (\rho e_T + p)v - u\tau_{xy} - v\tau_{yy} + q_y \end{bmatrix}.$$ (14)

Defining the flux tensor Π as

$$\Pi = \mathbf{E} \otimes \mathbf{i} + \mathbf{F} \otimes \mathbf{j},$$ (15)

where $\mathbf{i}$ and $\mathbf{j}$ are the unit vectors in the x and y-direction, Eq. (13) can be rewritten as

$$\frac{\partial \mathbf{U}}{\partial t} + \nabla \cdot \Pi = 0.$$ (16)

Integrating the above equation over the control volume V, and applying the divergence theorem to the right-hand side results

$$\frac{\partial}{\partial t} \int_V \mathbf{U} \, dV = -\int_V (\nabla \cdot \Pi) dV = -\int_S (\Pi \cdot \mathbf{n}) dS,$$ (17)

where S is the control surface that defines the control volume. Defining the volumetric mean of the vector $\mathbf{U}$ in the control volume V as

$$\overline{\mathbf{U}} \equiv \frac{1}{V} \int_V \mathbf{U}\, dV \,, \qquad (18)$$

Eq. (17) is written as

$$\frac{\partial \overline{\mathbf{U}}}{\partial t} = -\frac{1}{V} \int_S (\Pi \cdot \mathbf{n})\, dS \,, \qquad (19)$$

where $\mathbf{n}$ is the unit vector normal to the surface S.

For the volume (i, j), the first-order approximation of the temporal derivative is given by

$$\left(\frac{\partial \overline{\mathbf{U}}}{\partial t} \right)_{i,j} = \frac{\Delta \overline{\mathbf{U}}_{i,j}}{\Delta t} + O(\Delta t), \qquad (20)$$

and the temporal approximation of Eq. (19) for a quadrilateral and two-dimensional control volume is

$$\Delta \overline{\mathbf{U}}_{i,j} = -\frac{\Delta t}{V_{i,j}} \left[\int_{S_{i+1/2}} (\Pi \cdot \mathbf{n})\, dS + \int_{S_{i-1/2}} (\Pi \cdot \mathbf{n})\, dS + \int_{S_{j+1/2}} (\Pi \cdot \mathbf{n})\, dS + \int_{S_{j-1/2}} (\Pi \cdot \mathbf{n})\, dS \right], \qquad (21)$$

where $S_{i+1/2}$ is the common surface between volume (i, j) and volume $(i+1, j)$. Defining the function of the flux of tensor Π over the control surface S as

$$\mathcal{F}\left(\overline{\mathbf{U}} \right)_{i,j} = \frac{\Delta t}{V_{i,j}} \left[(\Pi \cdot \mathbf{S})_{i+1/2} + (\Pi \cdot \mathbf{S})_{i-1/2} + (\Pi \cdot \mathbf{S})_{j+1/2} + (\Pi \cdot \mathbf{S})_{j-1/2} \right], \qquad (22)$$

the spatial approximation of Eq. (21) is

$$\Delta \overline{\mathbf{U}}_{i,j} = -\left[\mathcal{F}\left(\overline{\mathbf{U}} \right)_{i,j} - \mathcal{D}\left(\overline{\mathbf{U}} \right)_{i,j} \right] \,, \qquad (23)$$

where $\mathcal{D}\left(\overline{\mathbf{U}} \right)_{i,j}$ is an artificial dissipation. It is important to note that Eq. (23) is a spatial approximation of Eq. (21) because tensor Π is considered constant over each of the four control surfaces that define the control volume.

In order to calculate $\mathcal{F}\left(\overline{\mathbf{U}} \right)_{i,j}$, the flux of tensor Π through the control surfaces must be calculated. For the surface $\mathbf{S}_{i+1/2}$, this flux is given by

$$(\Pi \cdot \mathbf{S})_{i+1/2} = \begin{bmatrix} \rho_{i+1/2}(q_S)_{i+1/2} \\ (\rho u)_{i+1/2}(q_S)_{i+1/2} + p_{i+1/2}(s_x)_{i+1/2} - \left[\mu_{i+1/2}(S_{xx})_{i+1/2}\right](s_x)_{i+1/2} - \left[\mu_{i+1/2}(S_{xy})_{i+1/2}\right](s_y)_{i+1/2} \\ (\rho v)_{i+1/2}(q_S)_{i+1/2} + p_{i+1/2}(s_y)_{i+1/2} - \left[\mu_{i+1/2}(S_{xy})_{i+1/2}\right](s_x)_{i+1/2} - \left[\mu_{i+1/2}(S_{yy})_{i+1/2}\right](s_y)_{i+1/2} \\ (\rho e_T)_{i+1/2}(q_S)_{i+1/2} + p_{i+1/2}(q_S)_{i+1/2} - u_{i+1/2}(s_x)_{i+1/2}\left[\mu_{i+1/2}(S_{xx})_{i+1/2}\right] - v_{i+1/2}(s_y)_{i+1/2}\left[\mu_{i+1/2}(S_{yy})_{i+1/2}\right] \\ - \left[v_{i+1/2}(s_x)_{i+1/2} + u_{i+1/2}(s_y)_{i+1/2}\right]\left[\mu_{i+1/2}(S_{xy})_{i+1/2}\right] \\ - \left[k_{i+1/2}(\partial T/\partial x)_{i+1/2}\right](s_x)_{i+1/2} - \left[k_{i+1/2}(\partial T/\partial y)_{i+1/2}\right](s_y)_{i+1/2} \end{bmatrix}. \qquad (24)$$

where the volumetric flux $(q_S)_{i+1/2}$ is defined by

$$(q_S)_{i+1/2} = \mathbf{u}_{i+1/2} \cdot \mathbf{S}_{i+1/2} = u_{i+1/2}(s_x)_{i+1/2} + v_{i+1/2}(s_y)_{i+1/2} \,, \qquad (25)$$

where $\mathbf{u}$ is the velocity vector.

It is important to note that the first terms in the right-hand side of Eq. (24) are the fluxes of mass, momentum and total energy through surface $\mathbf{S}_{i+1/2}$ and the other terms represents the fonts of momentum variation and total energy. In order to evaluate all this terms, in this work, it is used the fourth-order skew-symmetric scheme proposed by Ducros et al. (2000) given by

$$u_{i+1/2} = \frac{2}{3}\left(\underline{u}_i + \underline{u}_{i+1}\right) - \frac{1}{12}\left(\underline{u}_{i-1} + \underline{u}_i + \underline{u}_{i+1} + \underline{u}_{i+2}\right),$$ (26)

and

$$
\begin{aligned}
(\rho u)_{i+1/2} \equiv & \frac{1}{3}\left(\overline{\rho}_i + \overline{\rho}_{i+1}\right)\left(\underline{u}_i + \underline{u}_{i+1}\right) \\
& - \frac{1}{24}\left(\overline{\rho}_{i-1}\underline{u}_{i-1} + \overline{\rho}_{i+1}\underline{u}_{i-1} + \overline{\rho}_i\underline{u}_i + \overline{\rho}_{i+2}\underline{u}_i + \overline{\rho}_{i+1}\underline{u}_{i+1} \right. \\
& \left. + \overline{\rho}_{i-1}\underline{u}_{i+1} + \overline{\rho}_{i+2}\underline{u}_{i+2} + \overline{\rho}_i\underline{u}_{i+2}\right) \\
& + \frac{1}{3}\left[\frac{1}{2}\left(\overline{\rho}_{i+1}\underline{u}_{i+1} + \overline{\rho}_i\underline{u}_i\right) - \frac{1}{4}\left(\overline{\rho}_{i+1} + \overline{\rho}_i\right)\left(\underline{u}_{i+1} + \underline{u}_i\right)\right],
\end{aligned}
$$ (27)

since all calculated properties in the right-hand side of Eqs. (26) and (27) are volumetric means centered at the volume. The over bar indicates the volumetric mean defined by Eq. (19) and the under bar refers to the Favre mean, defined as

$$\underline{u} = \frac{\overline{\rho u}}{\overline{\rho}}.$$ (28)

The scheme proposed by Eqs. (27) and (28) is a centered one, and therefore, an explicit artificial viscosity must be included in Eq. (24). In order to enhance the numerical method with shock-capturing capabilities and the ability to cope with steep gradient regions, this artificial dissipation uses the basic idea proposed by Jameson et al. (1981) given by

$$\mathcal{D}\left(\overline{\mathbf{U}}\right) = \left[d_{i+1/2}\left(\overline{\mathbf{U}}\right) - d_{i-1/2}\left(\overline{\mathbf{U}}\right)\right] + \left[d_{j+1/2}\left(\overline{\mathbf{U}}\right) - d_{j-1/2}\left(\overline{\mathbf{U}}\right)\right],$$ (29)

where

$$d_{i+1/2}\left(\overline{\mathbf{U}}\right) = \varepsilon_{i+1/2}^{(2)}\left[\left(\overline{\mathbf{U}}\right)_{i+1} - \left(\overline{\mathbf{U}}\right)_i\right] - \varepsilon_{i+1/2}^{(4)}\left[\left(\overline{\mathbf{U}}\right)_{i+2} - 3\left(\overline{\mathbf{U}}\right)_{i+1} + 3\left(\overline{\mathbf{U}}\right)_i - \left(\overline{\mathbf{U}}\right)_{i-1}\right].$$ (30)

The first and second terms of Eq. (30) are a second-order and a fourth-order dissipation, respectively. The first term acts in the shock and the second term acts over steep gradient regions, like the viscous regions. The coefficients of Eq. (30) are given by

$$\varepsilon_{i+1/2}^{(2)} = \kappa^{(2)}\max\left(\Psi_i\Phi_i, \Psi_{i+1}\Phi_{i+1}\right), \quad \varepsilon_{i+1/2}^{(4)} = \max\left[0, \left(\kappa^{(4)} - \varepsilon_{i+1/2}^{(2)}\right)\right], \quad \kappa^{(2)} = 1/4, \quad \kappa^{(4)} = 1/256,$$ (31)

where the sensors Ψ_i and Φ_i are

$$\Psi_i = \frac{\left|\overline{p}_{i+1} - 2\overline{p}_i + \overline{p}_{i-1}\right|}{\left|\overline{p}_{i+1}\right| + \left|2\overline{p}_i\right| + \left|\overline{p}_{i-1}\right|}, \quad \Phi_i = \frac{\left(\nabla \cdot \underline{\mathbf{u}}\right)^2}{\left(\nabla \cdot \underline{\mathbf{u}}\right)^2 + \left|\nabla \times \underline{\mathbf{u}}\right|^2 + \varepsilon}, \quad \varepsilon = 10^{-30}.$$ (32)

The sensor Ψ_i is pressure-based and it is intended to detect the shock waves. The sensor Φ_i was proposed by Ducros et al. (1999), and its function is to inhibit sensor Ψ_i in regions were the divergent is low, but the rotational of the velocity field is high, like a pure vortex wake. In regions where the divergent and the rotational are high, like the vortex-shock interaction, the inhibiting capacity of sensor Φ_i decreases.

In order to advance Eq. (24) in time, a third-order Runge-Kutta is used as proposed by Shu (Yee, 1997). This yields to

$$\overline{\mathbf{U}}^1 = \overline{\mathbf{U}}^n - \left[\mathcal{F}\left(\overline{\mathbf{U}}^n\right) - \mathcal{D}\left(\overline{\mathbf{U}}^n\right) \right]$$

$$\overline{\mathbf{U}}^2 = \frac{3}{4}\overline{\mathbf{U}}^n + \frac{1}{4}\overline{\mathbf{U}}^1 - \frac{1}{4}\left[\mathcal{F}\left(\overline{\mathbf{U}}^1\right) - \mathcal{D}\left(\overline{\mathbf{U}}^1\right) \right] \tag{33}$$

$$\overline{\mathbf{U}}^{n+1} = \frac{1}{3}\overline{\mathbf{U}}^n + \frac{2}{3}\overline{\mathbf{U}}^2 - \frac{2}{3}\left[\mathcal{F}\left(\overline{\mathbf{U}}^2\right) - \mathcal{D}\left(\overline{\mathbf{U}}^2\right) \right]$$

As proposed in this work, the resulting numerical method is fourth-order accurate in space and third-order accurate in time.

4. Results

For all the cases studied in this work the Reynolds number is 10,000, and the characteristic length is the cord of the airfoil, c^*. The Mach number is 0.80 and the angle of attack ranges from 0 to 9 degrees. A c-grid is used, where the airfoil surface is discretized by 920 control volumes. The smallest grid size is $5.0 \times 10^{-4} c^*$, and it is located at the leading-edge surface. The grid extends $10c^*$ in the upper and lower normal directions, and approximately $10c^*$ in the upstream and downstream directions. The total number of control volumes for this grid is 324,000, resulting in a problem with 1,296,000 degrees of freedom.

Figure 1 shows a region of the computational domain in conjunction with a magnified view showing the resolution of the computational grid at the trailing edge, that has the same order of resolution that one at the leading edge. The angle of attack is $\alpha = 9^\circ$.
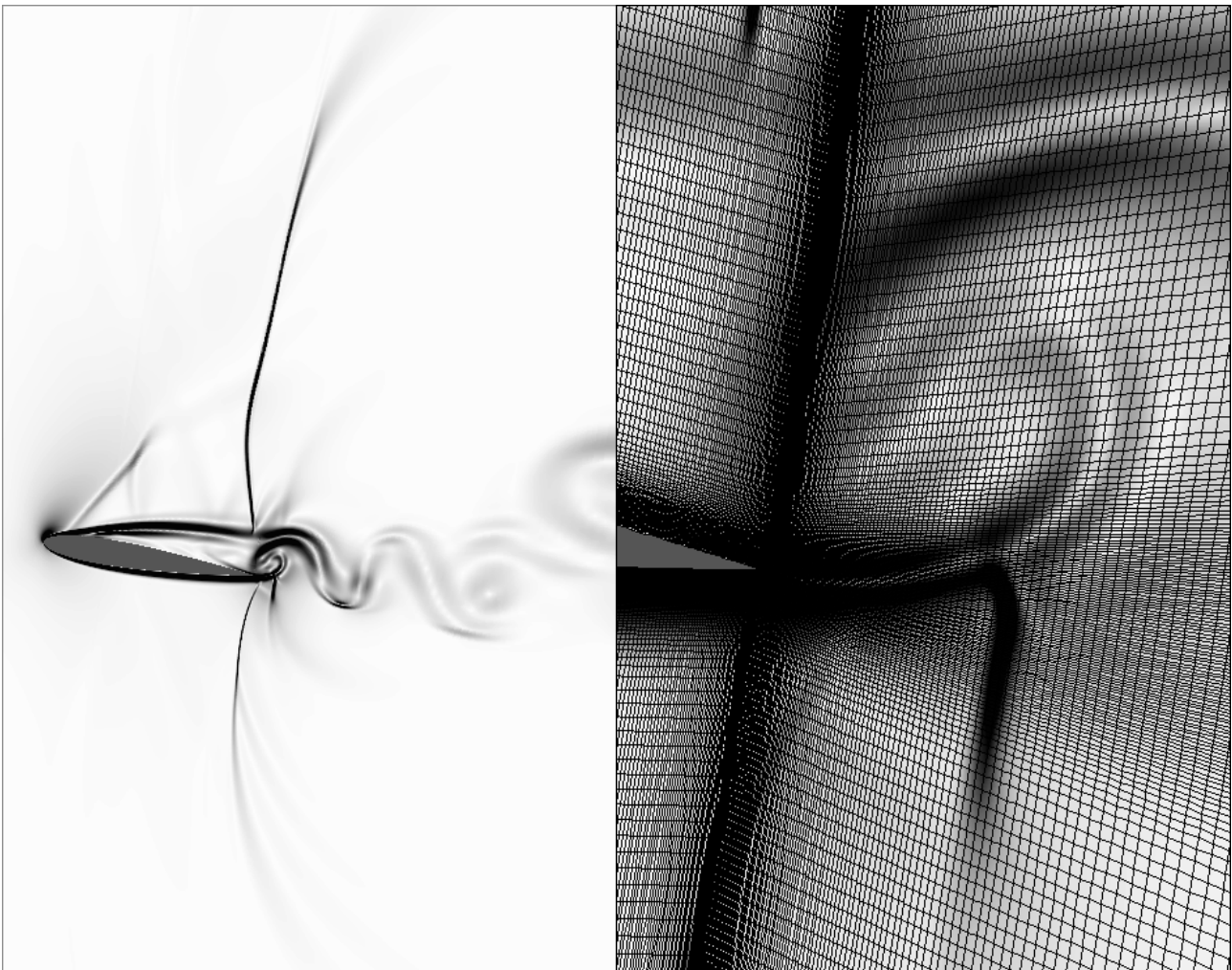
Figure 1. Flow visualization for $\alpha = 9^\circ$. The variable plotted is the nondimensional magnitude of the temperature gradient, $|\nabla T| = \sqrt{\left(\partial T/\partial x\right)^2 + \left(\partial T/\partial y\right)^2}$. White corresponds to 0.0 and black to 3.0.
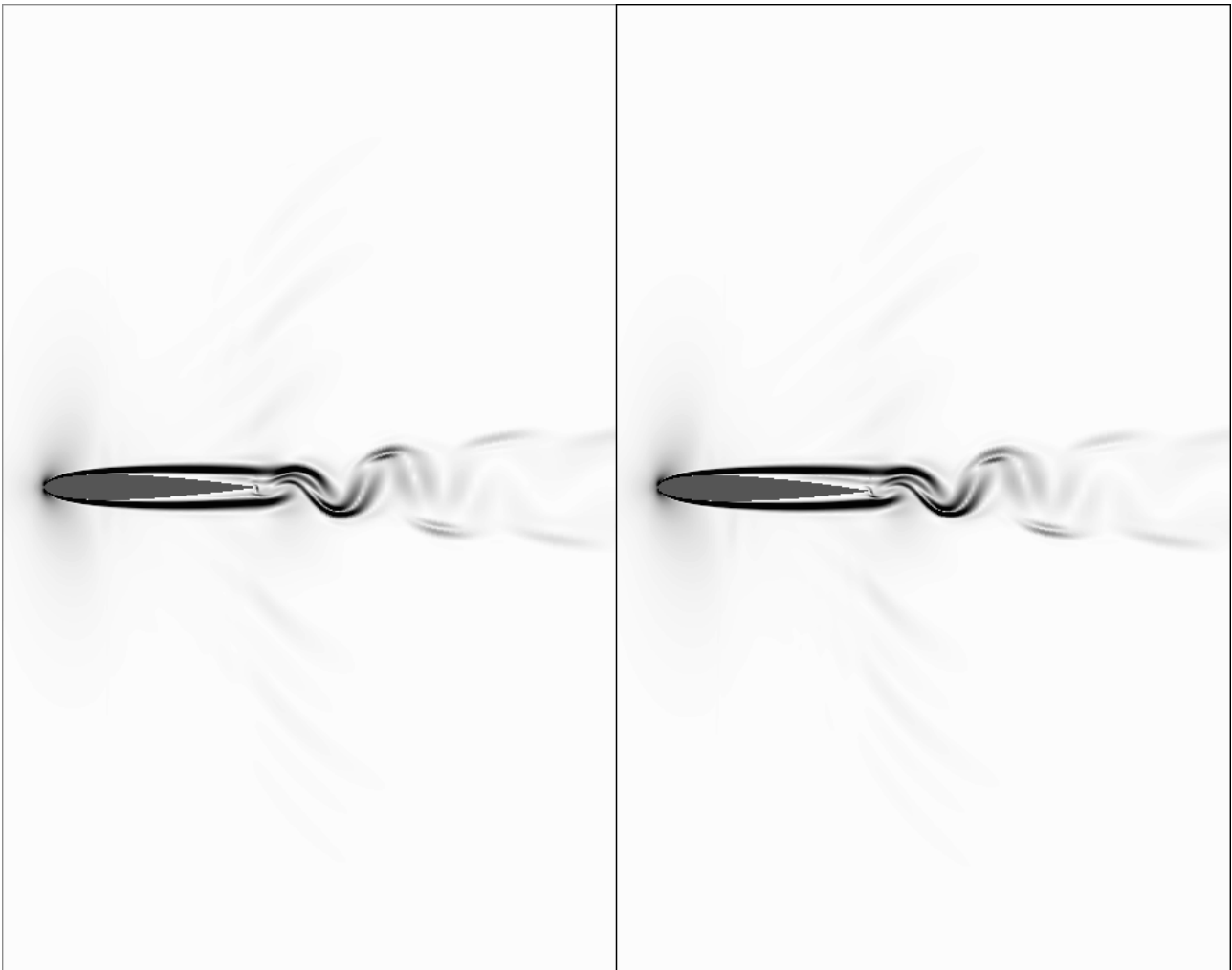
Figure 2. Flow visualization for $\alpha = 0^{\circ}$ (left) and $\alpha = 1^{\circ}$ (right). The variable plotted is the nondimensional magnitude of the temperature gradient, $|\nabla T| = \sqrt{(\partial T/\partial x)^2 + (\partial T/\partial y)^2}$. White corresponds to 0.0 and black to 3.0.
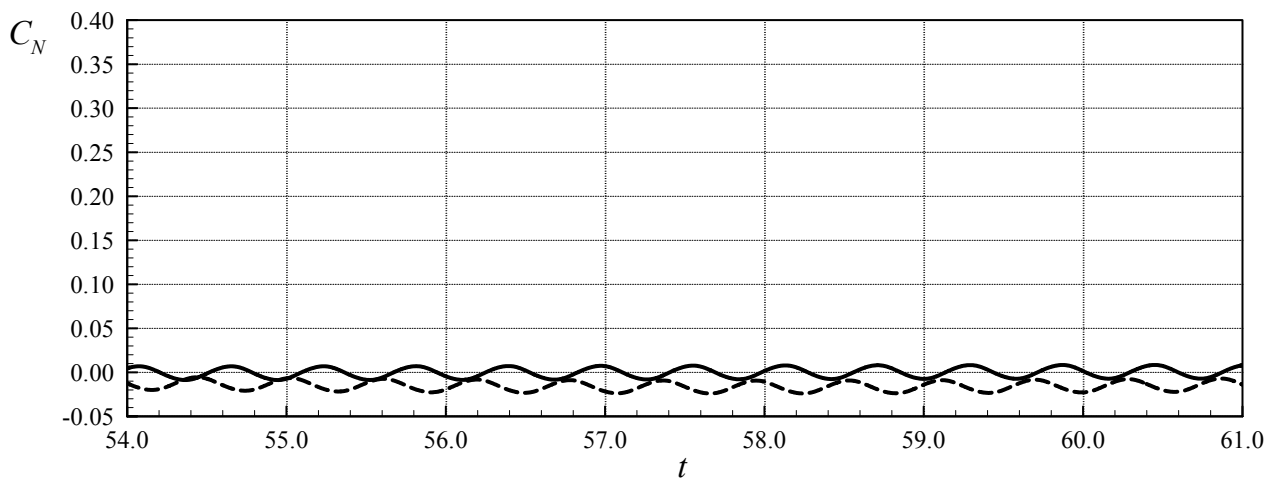
Figure 3. Normal-force coefficient, $C_N = 2N^*/\rho_\infty^* \left(U_\infty^*\right)^2$, as a function of the nondimensional time, $t = t^* U_\infty^* / c^*$, for $\alpha = 0^{\circ}$ (continuous) and $\alpha = 1^{\circ}$ (dashed).
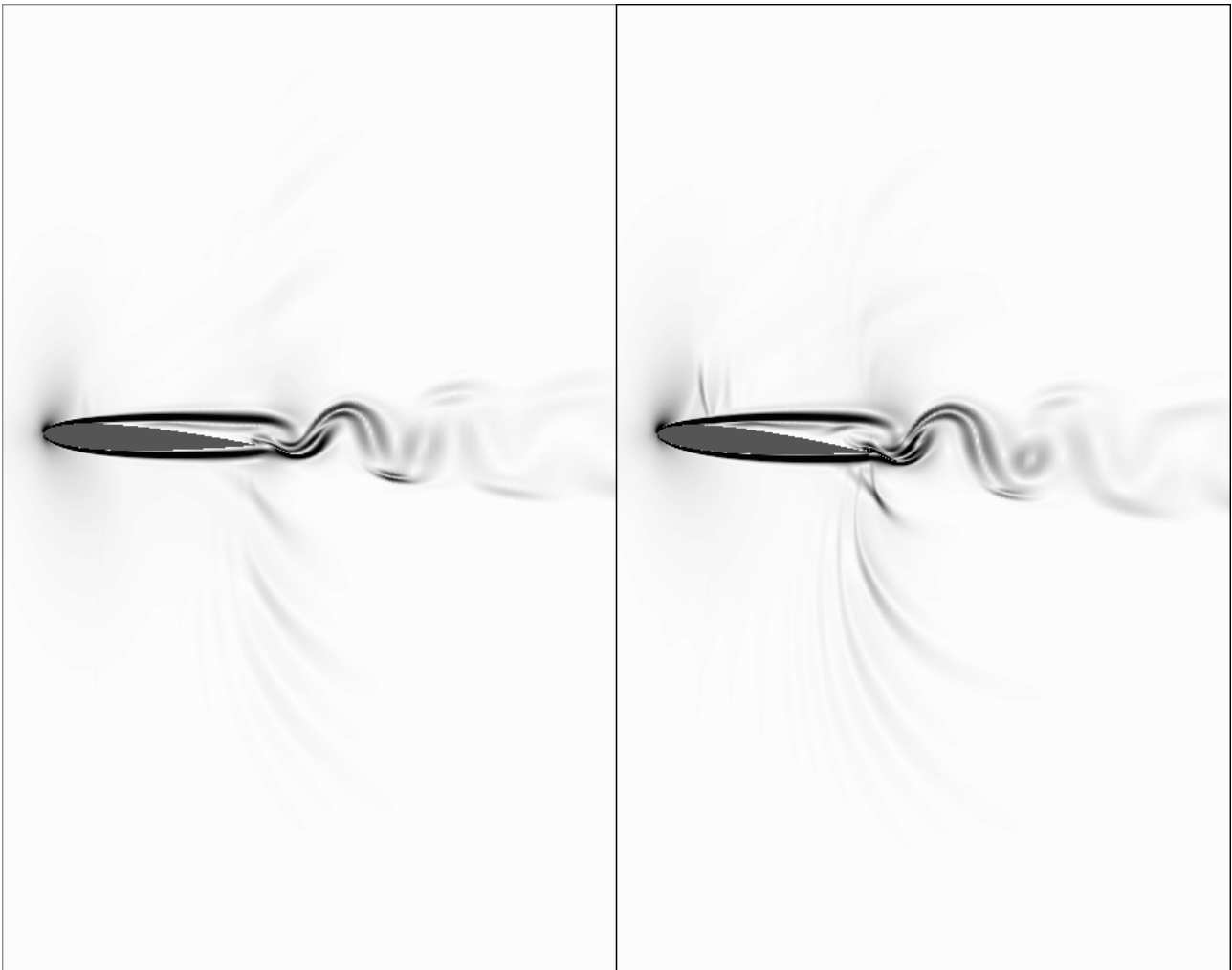
Figure 4. Flow visualization for $\alpha = 3^{\circ}$ (left) and $\alpha = 5^{\circ}$ (right). The variable plotted is the nondimensional magnitude of the temperature gradient, $|\nabla T| = \sqrt{(\partial T/\partial x)^2 + (\partial T/\partial y)^2}$. White corresponds to 0.0 and black to 3.0.
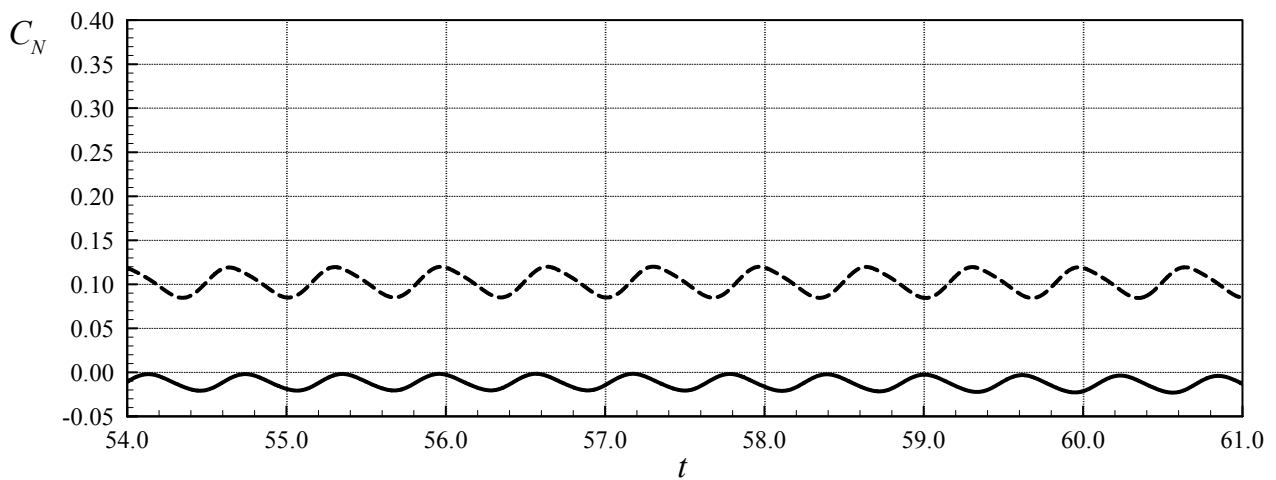
Figure 5. Normal-force coefficient, $C_N = 2N^* / \rho_\infty^* (U_\infty^*)^2$, as a function of the nondimensional time, $t = t^* U_\infty^* / c^*$, for $\alpha = 3^{\circ}$ (continuous) and $\alpha = 5^{\circ}$ (dashed).
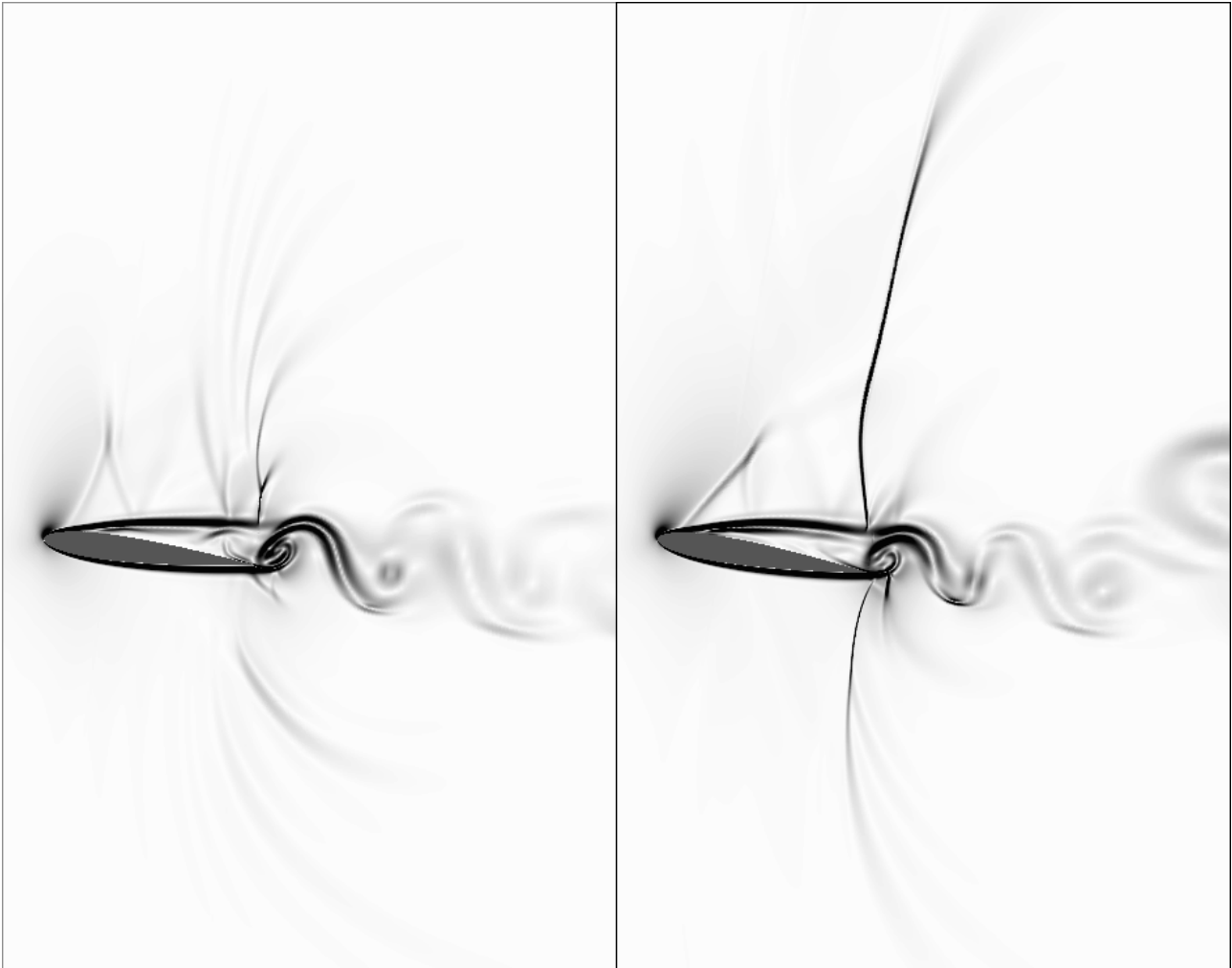
Figure 6. Flow visualization for $\alpha = 7^{\circ}$ (left) and $\alpha = 9^{\circ}$ (right). The variable plotted is the nondimensional magnitude of the temperature gradient, $|\nabla T| = \sqrt{(\partial T/\partial x)^2 + (\partial T/\partial y)^2}$. White corresponds to 0.0 and black to 3.0.
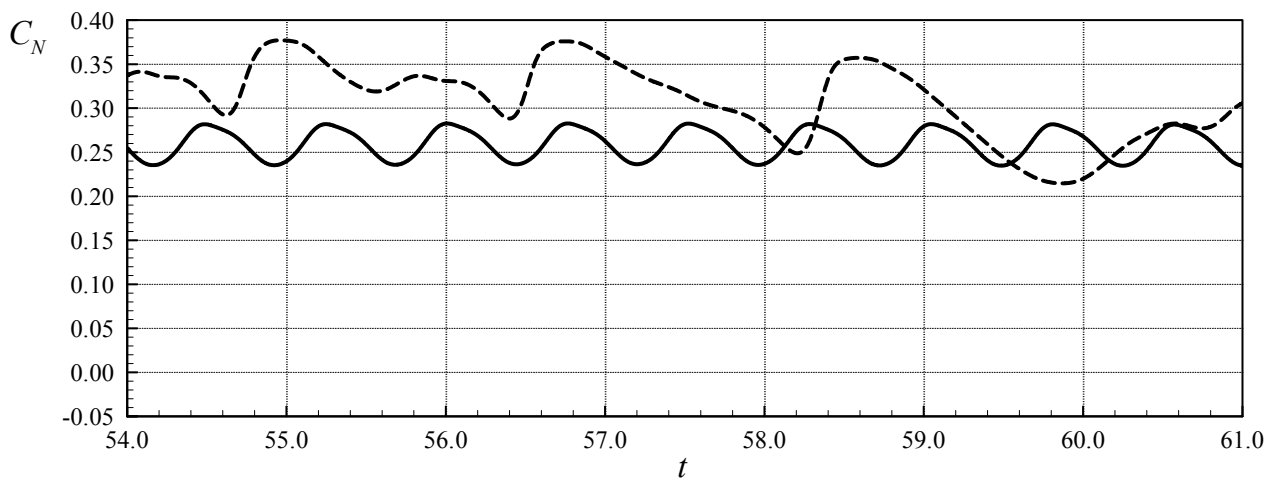
Figure 7. Normal-force coefficient, $C_N = 2N^* / \rho_\infty^* (U_\infty^*)^2$, as a function of the nondimensional time, $t = t^* U_\infty^* / c^*$, for $\alpha = 7^{\circ}$ (continuous) and $\alpha = 9^{\circ}$ (dashed).

For low angles of attack $\left(0^{o}, 1^{o} \text{ and } 3^{o}\right)$, as shown in Fig. 2 and in the left part of Fig. 4, the visualization shows the acoustics waves generated by a mild separation of the boundary layers along the upper and lower surface and the subsequent von Kármán's vortex street. As the angle of attack increases $\left(5^{o}, 7^{o} \text{ and } 9^{o}\right)$, as shown in right part of Fig. 4 and in Fig. 6, the acoustic waves turn into shock waves and a strong separation of the boundary layer is induced, generating a more complex vortex wake. Acoustic waves gave place to shock waves between 3° and 5° of angle of attack. Evidence of this is the appearance of the small lambda shocks in the upper and lower boundary layers presented in the right part of Fig. 4, corresponding to $\alpha = 5^{o}$.

The results also show a strong variation in the resultant unsteady aerodynamic coefficients. For the above mentioned low angles of attack, the unsteady normal-force coefficient is characterized by a characteristic amplitude and frequency, where the mean normal-force coefficient as a value that is very close to zero. For $\alpha = 5^{o}$, there is a jump in the mean value of normal force coefficient, as can be seen in Fig. 5, where the continuous line $\left(\alpha = 3^{o}\right)$ as a mean normal-force coefficient close to -0.01 and the dashed line $\left(\alpha = 5^{o}\right)$ has a normal-force coefficient close to 0.10. The amplitude also a significant increase, from 0.02 to 0.04, approximately. These variations are associated with the appearance of the small lambda-shocks in the upper and lower boundary layer.

The unsteady normal-force coefficient is similar in nature for $\alpha = 5^{o}$ (dashed line of Fig. 5) and $\alpha = 7^{o}$ (continuous line of Fig. 7). Variations are in the mean value and in the amplitude of the normal-force coefficient. For $\alpha = 9^{o}$, another departure is observed, associated with the formation of a very strong shock in the upper surface, as can be seen in the right part of Fig. 6. The unsteady normal-force coefficient is characterized by more than one characteristic frequency with an significant increase of its amplitude, as can be seen in Fig. 6 (dashed line).

5. Conclusions

The numerical simulation of the interaction between acoustic and shock waves with boundary layers that characterizes the laminar transonic flow over a NACA 0012 airfoil was performed. The results show that the nature of the compressibility effects, determined by the angle of attack, has a profound impact in the unsteady aerodynamic characteristics of the phenomena. For low angles of attack, where acoustic waves are predominant, the unsteady normal-force coefficient has a mean value very close to zero, associated with small amplitudes. As the angle of attack increases, small lambda-shocks substitute the acoustic waves, and the mean value of the normal-force coefficient rises significantly, as well as its amplitude. When strong shock-waves take the place of the small lambda-shocks, there is another departure, and the unsteady normal-force coefficient is characterized by more than one characteristic frequency and significant increase in the amplitude.

6. References

Anderson, D. A., Tannehill, J. C. and Pletcher, R. H., 1983, "Computational Fluid Mechanics and Heat Transfer", Hemisphe Publishing Corporation, New York, 599 p.

Bouhadji, A., and Braza, M., 2003, "Organized modes and shock-vortex interaction in unsteady viscous transonic flows around and airfoil Part I: Mach number effect", Computers and Fluids, Vol. 32, pp. 1233-1260.

Daru, V., and Tenaud, C., 2001, "Evaluation of TVD high resolution schemes for unsteady viscous shocked flows", Computers and Fluids, Vol. 30, pp. 89-113.

Ducros, F., Ferrand, V., Nicoud, F., Weber, C., Darraq, D., Gacherieu, C., Poinsot, T., 1999, "Large-Eddy Simulation of the Shock/Turbulence Interaction", Journal of Computational Physics, Vol. 152, pp. 517-549.

Ducros, F., Laporte, F., Soulères, T., Guinot, V., Moinat, P. and Caruelle, B., 2000, "High-Order Fluxes for Conservative Skew-Symmetric-like Schemes in Structured Meshes: Application to Compressible Flows", Journal of Computational Physics, Vol. 161, pp. 114-139.

Hirsch, C., 1988, "Numerical Computation of Internal and External Flows", Ed. John Wiley & Sons, Chichester, 515 p.

Jameson, A., Schmidt, W. and Turkel, E., 1981, "Numerical Solutions of the Euler Equations by Finite Volume Methods Using Runge-Kutta Time-Stepping Schemes", AIAA 14th Fluid and Plasma Dynamics Conference, AIAA-81-1259, Palo Alto, California.

Sandham, N. D., Li, Q. and Yee, H. C., 2002, "Entropy Splitting for High-Order Numerical Simulation of Compressible Turbulence", Journal of Computational Physics, Vol. 178, pp. 307-322.

Yee, H. C., 1997, "Explicit and Implicit Multidimensional Compact High-Resolution Shock-Capturing Methods: Formulation", Journal of Computational Physics, Vol. 131, pp. 216-232.

Yee, H. C., Sandham, N. D. and Djomehri M. J., B., 1999, "Low-Dissipative High-Order Shock-Capturing Methods Using Characteristic-Based Filters", Journal of Computational Physics, Vol. 150, pp. 199-238.

Yee, H. C., and Sjogreen, B., 2001, "Designing Adaptive Low-Dissipative High Order Schemes for Long-Time Integration", RIACS Technical Report 01.28.

Yee, H. C., Vinokur, M. and Djomehri M. J., B., 2000, "Entropy Splitting and Numerical Dissipation", Journal of Computational Physics, Vol. 162, pp. 33-81.